PAPER

Check for updates

Highly-robust nanoplate-shaped V_2O_5 as an efficient cathode material for aqueous zinc ion batteries

Priya Yadav,†[a] Ahmad Nurul Fahri, [ID] †[b] Jay Singh,[a] Ravinder Singh,[a] Jaekook Kim [ID] *[b] and Alok Kumar Rai [ID] *[a]

The efficiency and performances of energy storage and conversion systems are highly dependent on the electrode performances, which have a direct impact on their functioning. The fabrication of electrode materials with novel nanostructures has a substantial positive impact on their electrochemical performances. Recently, two-dimensional nanomaterials have drawn a lot of attention due to their significant features, such as distinctive 2D-layered structure and infinite planar lengths as well as providing short routes for ion and electron transportation including large surface areas for additional adsorption sites. Herein, we have proposed a simple solvothermal synthesis for the fabrication of 2D nanoplates of a V_2O_5 cathode for rechargeable aqueous zinc-ion batteries. The obtained high electrochemical results confirmed the potency of the V_2O_5 nanoplate cathode for zinc ion batteries. Furthermore, the Zn^{2+} ion storage mechanism within the V_2O_5 crystal lattice is also discussed, which is based on the phase transition from pristine V_2O_5 to zinc pyrovanadate ($Zn_xV_2O_5 \cdot nH_2O$) during reversible Zn^{2+} (de)-intercalation in the open-structured hosts.

Introduction

In today's modern civilization, the concerns related to energy storage, conversion, and distribution are crucial. An energy-storage device is considered to be ideal if it possesses the vital features of high safety, environmental friendliness, low cost, high specific capacity, fast charge/discharge capability, and high gravimetric and volumetric energy densities.[1–4] Lithium-ion batteries (LIBs) have garnered a lot of attention in recent years due to their numerous applications from small mobile gadgets to hybrid and electric cars. Despite the high energy and power density of LIBs, their wide-scale implementation is constrained by the safety risks caused by flammable organic electrolytes. In addition, the limited Li resources are also a major concern, which may restrict the further use of LIBs.[5–8] Recently, the rechargeable aqueous zinc-ion batteries have shown potential to be used as an alternative due to the low cost and high abundance of metallic zinc in the earth's crust (~2 USD per kg and ~75 ppm), excellent safety characteristics and low equilibrium redox potential (-0.76 V *vs.* SCE) of the Zn

electrode, and easy assembling procedures.[9–14] Similar to LIBs, the chemistry of aqueous zinc-ion batteries involves the movement of Zn^{2+} ions between the cathode and anode. The theoretical capacity of metallic zinc is ~820 mA h g^{-1} and it has a high kinetic overpotential for hydrogen evolution, which makes it stable with an aqueous electrolyte.[9–12] Despite many advantages of the zinc metal as an anode, a suitable cathode material is highly required, which is currently restricting the advancement of rechargeable Zn-ion batteries. Various cathode materials for aqueous Zn-ion batteries are currently under investigation, such as Prussian blue analogues,[15] polyanion metal phosphates,[16] quinone analogues,[17] manganese dioxide,[18] vanadium-based compounds, *etc.*[19] However, the undesirable phase transitions, co-insertion of H$^+$ along with Zn^{2+}, structural failure and material disintegration were found to be major drawbacks associated with cathode materials.[15–21] Thus, to select a novel cathode material with high reversible capacity and a long cycle life is still a challenge for aqueous zinc ion batteries.

Recently, the V_2O_5 electrode material was identified as a promising cathode due to its high specific capacity (~589 mA h g^{-1}), rich resources, layered structure with a stable open-framework, steady cycling performance and outstanding rate capability. However, the structural instability during long-term cycling and the low electrical conductivity are still unresolved issues of the V_2O_5 cathode.[19–23] Among all the approaches to optimize these issues, the priority is given to the fabrication of novel nanostructures, which in fact offers numerous intriguing properties such as more active sites for redox reactions, short diffusion paths for Zn^{2+} ions, high surface area and

a Department of Chemistry, University of Delhi, Delhi-110007, India.
 E-mail: alokkumarrai1@gmail.com, akrai@chemistry.du.ac.in
b Department of Materials Science and Engineering, Chonnam National University,
 300 Yongbong-dong, Bukgu, Gwangju, 500-757, Republic of Korea.
 E-mail: jaekook@chonnam.ac.kr
† These authors contributed equally to this manuscript.

large electrode/electrolyte contact area, as well as suppresses the structural breakdown to a certain extent induced by volume changes, resulting in excellent electrochemical performances.

Thus, we have fabricated here a two-dimensional (2D) nanoplate-shaped V_2O_5 cathode material using a facile solvothermal synthesis method and tested its suitability for aqueous zinc ion batteries. Recently, 2D nanomaterials have been significantly used as electrode materials for energy storage applications due to their high mechanical integrity as they are stacked by van der Waals forces and made up by the substantial overlapping of the layers. In addition, the major advantages regarding atomic arrangement, coordination number, bond lengths, atomic or molecular thickness and infinite planar lengths of 2D nanomaterials make them superior to their bulk counterparts.[24,25] The obtained results demonstrate that the electrochemical performances of a nanoplate-shaped V_2O_5 cathode at high current rate are still stable. This research is expected to provide a feasible strategy for designing and creating promising vanadium-based cathode materials for rechargeable aqueous zinc-ion batteries.

Experimental

Material synthesis

Initially, 6 mmol of vanadium acetylacetonate (Sigma Aldrich, India, 97%) was dissolved in 30 mL each of anhydrous carbinol and ethylene glycol under continuous stirring. Thereafter, liquid ammonia (NH_4OH) was added dropwise to maintain pH $\sim$ 9 in the above precursor solution under vigorous stirring. Then, after continuous stirring for 45 min, the obtained solution was further transferred to a Teflon-lined stainless-steel autoclave and heated up to 180 °C for 12 h. The as-prepared product was collected after natural cooling followed by centrifugation and washing with distilled water and ethanol several times to remove the organic impurities. After overnight drying of the as-prepared sample at 80 °C, the calcination was performed in an air atmosphere at 450 °C for 1 h with the heating rate of 1° min^{-1}.

Material characterisation

The crystallinity and purity of the calcined sample was determined by X-ray diffraction analysis (XRD, Shimadzu X-ray diffractometer with Cu Kα radiation, λ = 1.5406 Å). The surface morphology, particle size, and shape of the calcined sample were analyzed by field-emission scanning electron microscopy (FE-SEM, S-4700 Hitachi) and field emission transmission electron microscopy (FE-TEM, Philips TecnaiF20 at 200 kV). Furthermore, the elemental mapping and surface chemical compositions of the calcined sample were characterized by energy dispersive spectroscopy (EDS) and X-ray photoelectron spectroscopy (XPS; M/s Thermo Fischer Scientific Instrument UK with a monochromatic Al Kα X-ray source), respectively. Raman analysis was carried out using a Renishaw Raman Microscope, with a 514 nm laser to analyse the chemical bonding states of the product. The surface area including pore size distribution was investigated by the Brunauer–Emmett–Teller method using N_2 adsorption/desorption isotherms (BET, Micromeritics Instrument Corp. Gemini-V).

Electrode fabrication

A CR-2032 coin-type half-cell of the V_2O_5 cathode was assembled using zinc metal foil as a reference electrode, glass fibre as a separator and 2 M $ZnSO_4$ as an electrolyte. Initially, to fabricate a working electrode, the active materials (70 wt%), acetylene black (15 wt%) and polyacrylic acid (PAA) (15 wt%) were pressed onto a stainless-steel mesh, which was then dried under vacuum at 120 °C for 12 h. The cells were assembled in an open air environment and they were ideally kept for 12 h for aging before the electrochemical measurements. The electrochemical measurements were performed using a WBCS 3000 (WonATech) battery tester between the potential
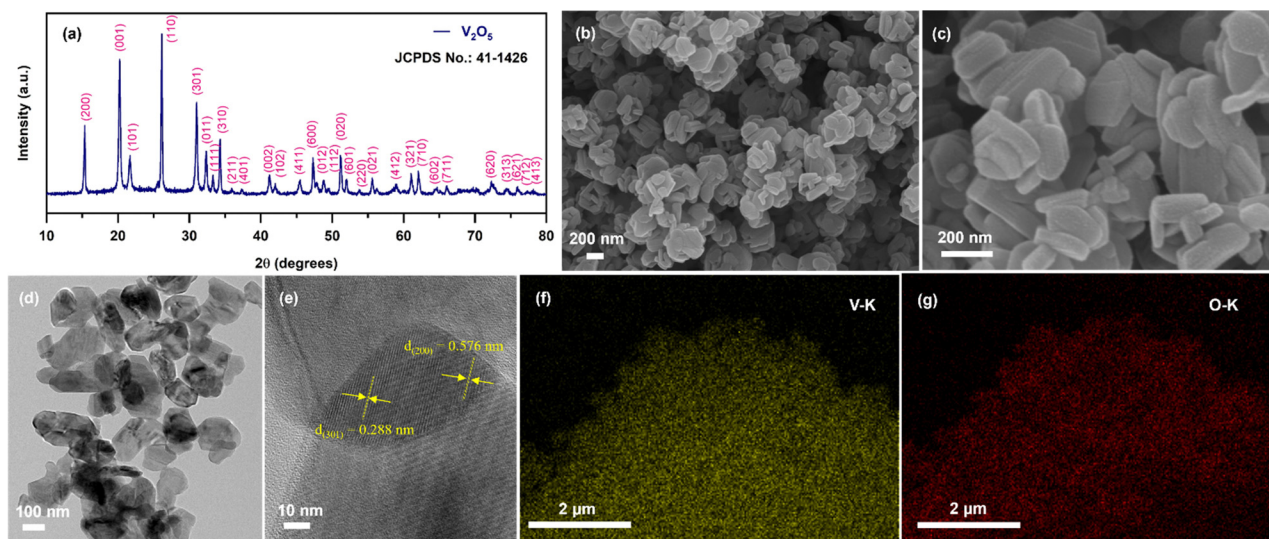

Fig. 1 (a) XRD pattern; (b, c) FE-SEM images at different magnifications; (d) FE-TEM image; (e) HR-TEM image; and (f, g) representative EDX mapping images of the V_2O_5 sample.

range of 0.2–1.6 V. Cyclic voltammetry (CV) was also carried out using an AUTOLAB PGSTAT302N potentiostat for the initial five cycles at the constant scan rate of 0.2 mV s^{-1} under the same potential range.

Results and discussion

Physiochemical properties

Fig. 1(a) shows the XRD pattern of the calcined sample, which clearly demonstrates sharp peaks with high intensity, indicating high crystallinity of the sample. All the diffraction peaks of the sample are well consistent with the standard diffraction pattern of the orthorhombic phase of V_2O_5 with *Pmmn* space group (JCPDS no: 00-041-1426). In addition, there were no other impurity peaks visible in the diffraction pattern, which implies that the calcined sample is highly pure. The morphological analysis of the calcined sample was then further investigated and the obtained results are shown in Fig. 1(b)–(d). Fig. 1(b) and (c) represent the FE-SEM images taken at different

magnifications, which clearly shows 2D nanoplate-type morphology. As can be seen from the figure, the nanoplates are highly aggregated with smooth surfaces. As shown in Fig. 1(d), TEM analysis was also performed for detailed microstructural analysis. The obtained TEM image is in accordance with the FE-SEM results. The nanoplate sizes are in the range of ~50–200 nm. The high-resolution TEM (HR-TEM) image displayed in Fig. 1(e) indicates the high-crystallinity of the calcined sample. The HR-TEM image demonstrates clear lattice fringes with interplanar spacing of ~0.571 nm and 0.288 nm, corresponding to the (200) and (301) planes respectively, which is matched with the XRD pattern of the V_2O_5 sample. The elemental-mapping images displayed in Fig. 1(f) and (g) confirmed the uniform dispersion of vanadium (V-K; yellow) and oxygen (O-K; red) elements without the existence of any other impurities throughout the sample, which indicates that the nanoplates are mainly composed of V_2O_5.

In order to investigate the oxidation states of the elements, XPS analysis was carried out and the obtained results are displayed in Fig. 2(a) and (b). Fig. 2(a) shows the survey
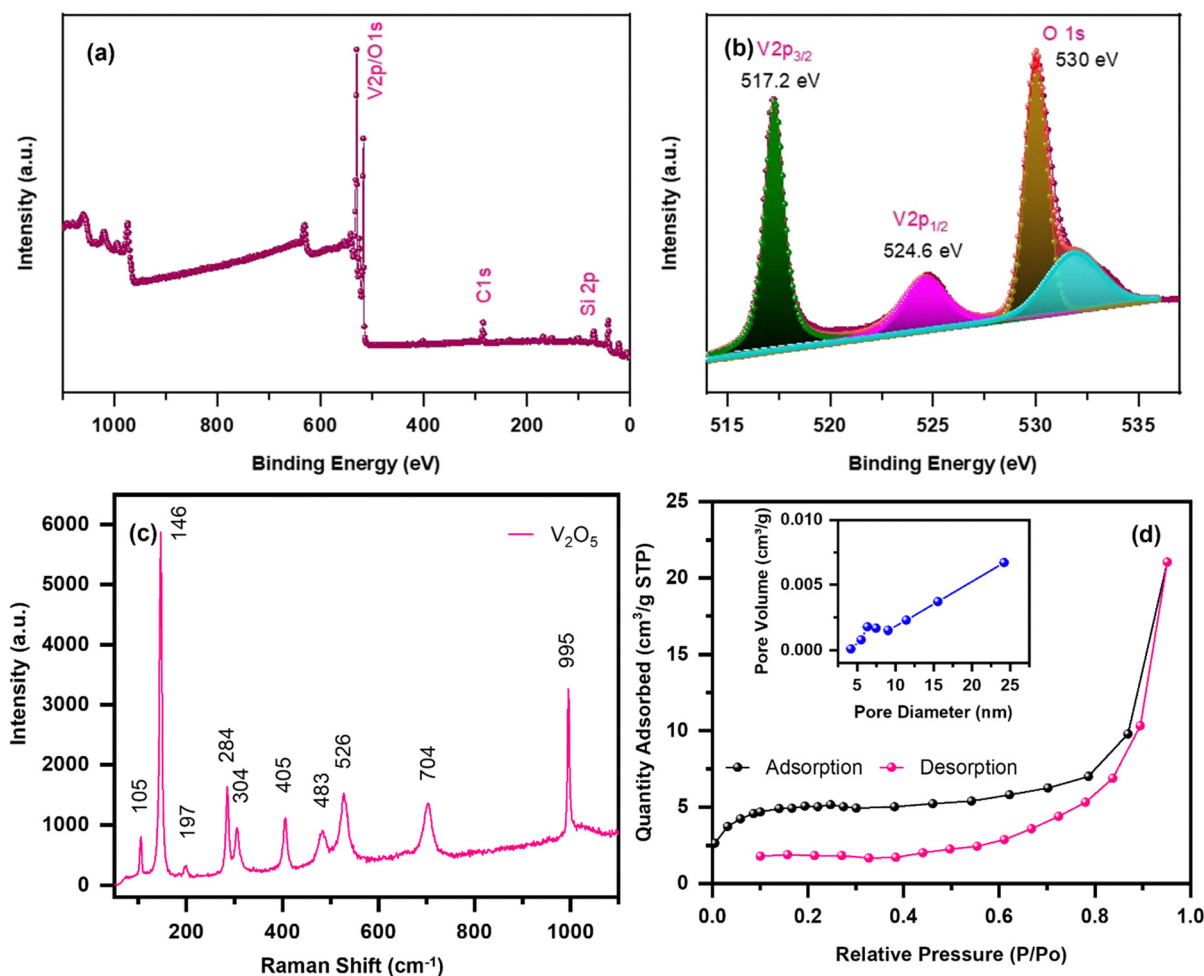

Fig. 2 XPS: (a) survey spectrum; (b) V-2p and O-1s spectrum; (c) Raman spectrum; (d) BET analysis with pore size distribution (inset) of the nanoplate-shaped V_2O_5 sample.

spectrum of the calcined V_2O_5 sample, which clearly shows the presence of vanadium (V) and oxygen (O) elements. More precisely, Fig. 2(b) represents the combined de-convoluted XPS spectra of V-2p and O-1s. As can be seen, the characteristic peaks obtained at binding energies of 517.2 and 524.6 eV correspond to V^{5+} $2p_{3/2}$ and $2p_{1/2}$, respectively. Since the binding energy difference between the core levels is found to be 7.4 eV, it is in good agreement with the electronic states of V_2O_5. The peaks located at binding energies of 530 eV and 531.9 eV of the O-1s spectrum belong to the V–O and V–OH bonds of the V_2O_5 sample.[26,27] Raman analysis is also employed to investigate the bonding configurations using a variety of molecular vibrational modes, as shown in Fig. 2(c). The Raman spectrum was measured in the Raman shift range of 50–1100 cm^{-1}, which exhibits various high and intense peaks located at ~105, ~146, ~197, ~284, ~304, ~405, ~483, ~526, ~704 and ~995 cm^{-1}. The peaks present at 146 and 197 cm^{-1} are related to the B_{3g} mode of V–O–V chains, which indicates the relative motion of V_2O_5 layers with regard to one another, indicating high crystallinity of the sample. However, the other two peaks present at 284 and 405 cm^{-1} show the bending vibration of V=O type bonding. On the other hand, the shoulder peaks obtained at 483 and 304 cm^{-1} belong to bending vibrations of V–O–V (doubly coordinated oxygen) and V_3–O (triply coordinated oxygen) type, respectively.[28,29] The peaks positioned at 526 and 704 cm^{-1} correspond to the stretching vibrations of triply co-ordinated oxygen (V_3–O) and doubly co-ordinated oxygen (V_2–O), respectively. Finally, the Raman shift present at 995 cm^{-1} is due to the terminal oxygen (V^{5+}=O) stretching mode.[29,30] In addition, BET analysis was also conducted to evaluate the specific surface area and porosity of the material. As depicted in Fig. 2(d), the N_2 adsorption–desorption isotherms show a type IV isotherm, indicating mesoporosity in the sample. The BET surface area was found to be 15.94 m^2 g^{-1}. Moreover, the Barrett–Joyner–Halenda (BJH) pore size distribution plot, as shown in the inset of the figure, demonstrates an average pore diameter of ~16.8 nm and total pore volume of ~0.032 cm^3 g^{-1}, which also suggests that the material possesses mesopores. It is well known that a porous nanostructure and large surface area offers a short diffusion length, better electrolyte impregnation, numerous active sites for Zn-ion adsorption, *etc.*, and thereby excellent electrochemical performances.[30]

Electrochemical investigation

Fig. 3 displays CV curves for the initial 5 cycles at a constant scan rate of 0.2 mV s^{-1}. As can be seen, the first cycle shows two reduction peaks located at ~0.57 V and ~0.9 V, which is due to the insertion processes of Zn-ions in the V_2O_5 nanoplate electrode. During the anodic scan, the oxidation peaks observed at ~1.08 and ~1.35 V can be attributed to the de-insertion of Zn^{2+} ions.[31] However, compared to the first cycle, the peak positions and peak current from the second cycle onwards are different, which may be due to the incomplete extraction of inserted Zn^{2+} ions from the V_2O_5 nanostructure.[19] In addition, the cathodic peak observed at ~0.9 V in the first

cycle splits into two peaks during the second cycle and appeared to be ~0.91 V and ~1.1 V, which could be described by the multiple insertion reactions of Zn^{2+} ions because of the chemical defects of vanadium oxide.[32] The peak located at ~0.91 V and ~0.57 V corresponds to the redox reaction of V^{5+}/V^{4+} and V^{4+}/V^{3+}, respectively.[33]

Furthermore, the charge/discharge data of the V_2O_5 electrode was recorded at a constant current density of 0.5 A g^{-1} for the initial 15 cycles. And out of 15 cycles, Fig. 3(b) shows the charge/discharge curves of the 1st, 2nd, 3rd, 4th, 5th and 10th cycles. Though the voltage profiles are similar, the high reversibility and stability can be easily seen in all the cycles except for the first discharge cycle of the electrode material. The significant irreversible capacity loss observed in the initial discharge cycle can be attributed to the formation of the SEI layer, which causes the kinetic limitations by consuming more number of Zn^{2+} ions during discharge, but does not allow extraction of the same number of Zn^{2+} ions during charge.[19,34] It is clear from the figure that from the second cycle onwards, the voltage profile shows high reversibility, which indicates a decrease in charge transfer resistance at the electrode/electrolyte contact, resulting in low polarization. The small polarization demonstrates fast Zn^{2+} transfer kinetics within the electrode. The electrode is able to deliver the charge/discharge capacities of ~141.2/170.06, ~132.2/137.38, ~123.7/124.26, ~127.8/126.26, ~132.2/132.03 and ~141.06/143.46 mA h g^{-1} for the 1st, 2nd, 3rd, 4th, 5th and 10th cycles, respectively, which clearly indicates ~100% coulombic efficiency of the electrode. On the other hand, Fig. 3(c) represents the galvanostatic charge/discharge cycles of the V_2O_5 electrode for the 30th, 60th, 100th, 500th and 1000th cycles at a constant current density of 5 A g^{-1}. It can be observed that the capacity decreases with increase of the cycle numbers. However, the coulombic efficiency was still ~100% throughout the cycling and the charge/discharge capacity was found to be ~69/69.8 mA h g^{-1}, ~67.8/68.8 mA h g^{-1}, ~63.40/61.34 mA h g^{-1}, 56.34/56.34 mA h g^{-1} and ~43.81/43.81 mA h g^{-1}, respectively for the above-mentioned cycle numbers. In addition, it is also believed that the high surface area along with the electrode may also tolerate the absolute volume changes of the electrode during the insertion/de-insertion of Zn^{2+} ions. In order to investigate the stability of the nanoplate-shaped V_2O_5 electrode, C-rate was performed at various current densities of 0.5 A g^{-1} to 20 A g^{-1} and the obtained results are displayed in Fig. 3(d). The V_2O_5 cathode delivers the specific capacities of ~183, ~168, ~156, ~133, ~104 and ~59 mA h g^{-1} at current densities of 0.5, 1, 2, 5, 10 and 20 A g^{-1}, respectively. Impressively, when the current rate returns back to the initial current rate of 0.5 A g^{-1} after 60 cycles, the electrode is still able to regain the original capacity of ~180 mA h g^{-1} with ~100% coulombic efficiency, which clearly indicates the high stability of the electrode material. In addition, the continuous capacity loss with increase of the current density during cycling is a common phenomenon as Zn^{2+} ions do not get sufficient time to (de)-intercalate at high current rates.[35,36] More importantly, it can be seen that the electrode exhibits 32% of the initial capacity at such a high current density of 20 000 mA g^{-1} (20 A g^{-1}), which also suggests that the nanoplate morphology maintains the integrity of

the electrode during volume expansion/contraction resulting from Zn^{2+} (de)-insertion. Fig. 3(e) shows the specific capacity *versus* cycle number graph including the corresponding coulombic efficiency data of the 2D nanoplate-shaped V_2O_5 electrode at the current density of 0.5 A g^{-1} for the first 15 cycles followed by 5 A g^{-1} fo a further 1000 cycles. Since the electrode

delivers the initial discharge/charge capacity of $\sim$180/141 mA h g^{-1}, the capacity was maintained at $\sim$44 mA h g^{-1} after 1000 cycles. Significant capacity loss can be noticed after 15 cycles and the capacity reaches $\sim$75 mA h g^{-1}, which can be ascribed to the fact that the inserted Zn^{2+} ions could not be completely extracted from the V_2O_5 lattice. These unextracted Zn^{2+} ions locate at the "dead Zn^{2+}
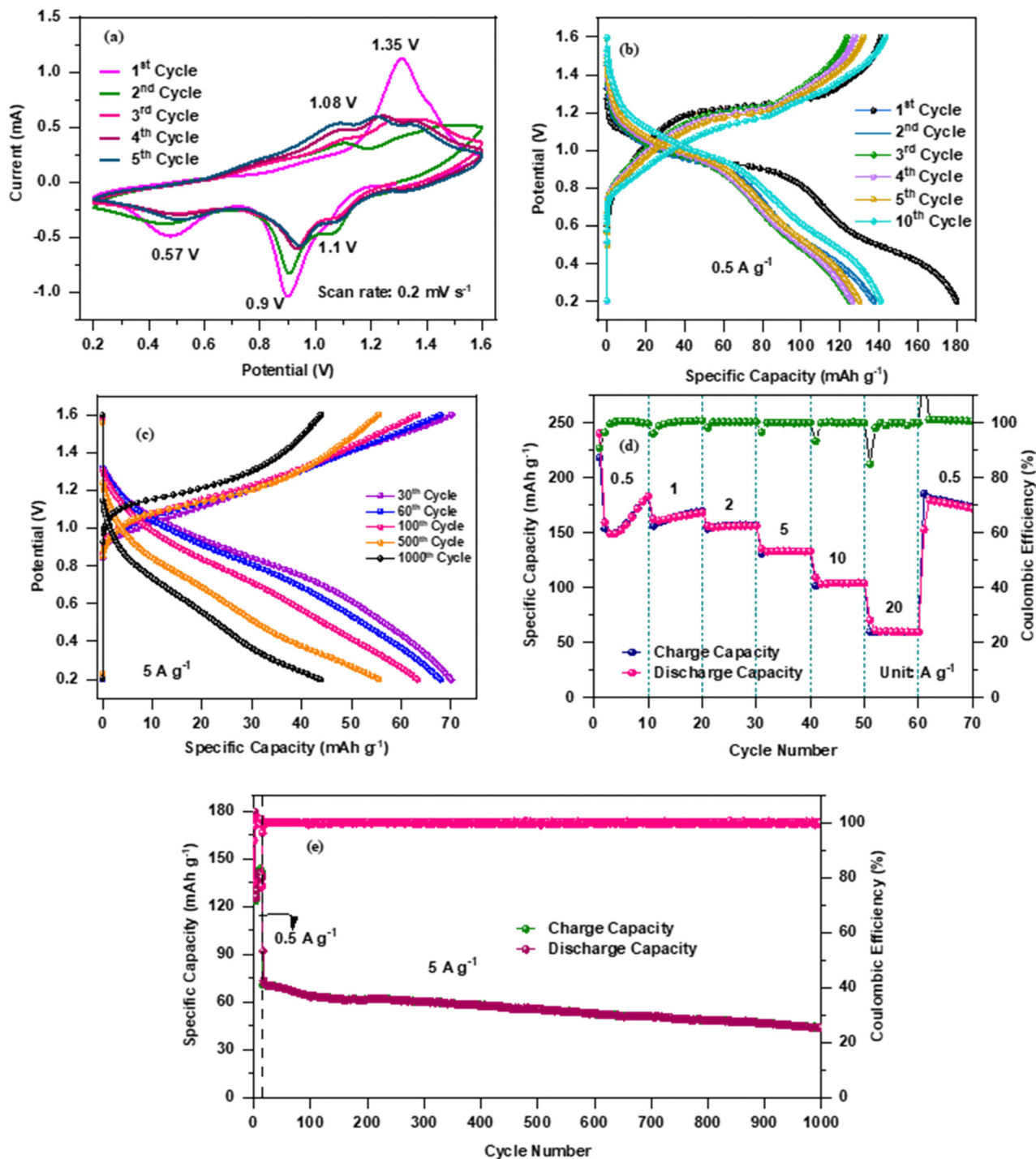

Fig. 3 (a) Cyclic voltammetry curves at a constant scan rate of 0.2 mV s^{-1}; (b) discharge/charge curves at a current density of 0.5 A g^{-1} for the initial five cycles; (c) discharge/charge curves at a current density of 5 A g^{-1} for 1000 cycles; (d) C-rate performance at different current densities and (e) cycling performance at a constant current density of 5 A g^{-1} until 1000 cycles of the nanoplate-shaped V_2O_5 electrode.
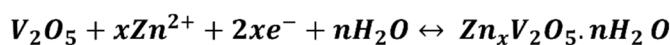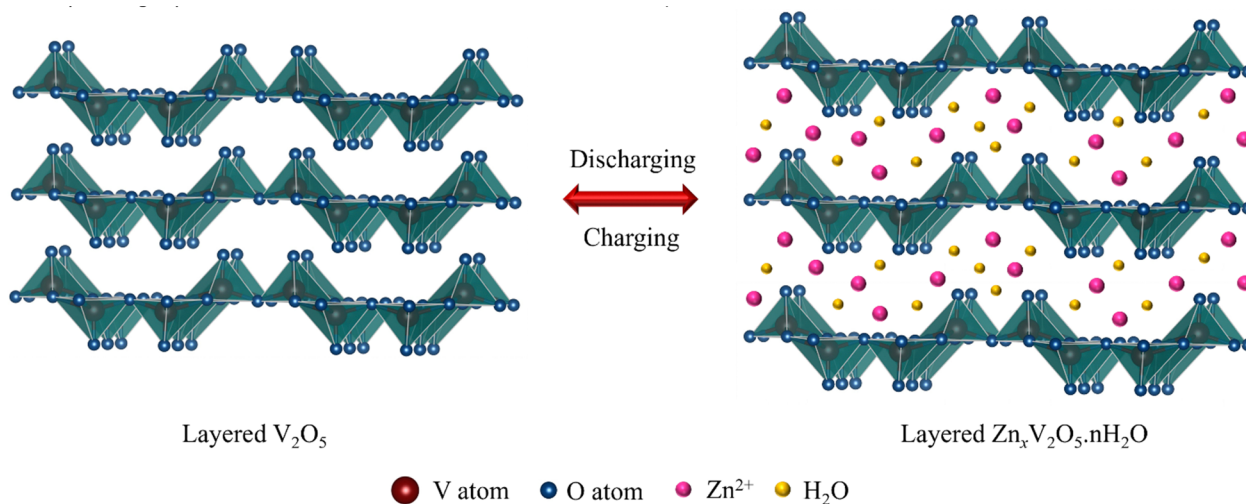
$$V_2O_5 + xZn^{2+} + 2xe^- + nH_2O \leftrightarrow Zn_xV_2O_5 \cdot nH_2O$$

Fig. 4 Schematic illustration of the Zn-ion storage mechanism in the layered V_2O_5 crystal system.

sites'' making the layered crystalline structure stable with promising stable capacity until 1000 cycles.[2,23] The layered V_2O_5 cathode permits a high extent of reversibility for hydrated Zn^{2+} (de)-intercalation. It is believed that the co-insertion of H_2O along with Zn^{2+} ions causes structural evolution and changes the layered V_2O_5 into a layered $Zn_xV_2O_5 \cdot nH_2O$. On the other hand, the subsequent charging process enables the reversal of the structural evolution followed by the extraction of hydrated Zn^{2+} ions that have occurred during discharge. The co-intercalated H_2O molecules act as a buffer against the high charge density of Zn^{2+}, which facilitates quick cation transfer and high-rate capability. The reversible reaction of the Zn–V_2O_5 battery is schematically illustrated in Fig. 4 with the corresponding equation.[37]

Conclusions

Herein, we have fabricated a 2D nanoplate-shaped V_2O_5 cathode material through a facile solvothermal method. The electrochemical investigation results clearly demonstrate that the V_2O_5 electrode exhibits high specific capacity and better rate capability even at a high current density of 20 A g^{-1}. The excellent performance of the V_2O_5 electrode can be attributed to the unique features of the nanoplates *i.e.*, larger specific surface area and high mechanical stability, which increases the conductivity by shortening the diffusion paths for ions. The cathode delivers an initial charge capacity of ~ 141 mA h g^{-1} at a current density of 0.5 A g^{-1} and retains a capacity of ~ 44 mA h g^{-1} after 1000 cycles at a current density of 5 A g^{-1}. The obtained results conclude that the high performance of the V_2O_5 nanoplates provides potential feasibility as a cathode material for ZIBs.

Conflicts of interest

There are no conflicts to declare.

Acknowledgements

References

1 J. M. Tarascon and M. Armand, *Nature*, 2008, **451**, 652–657.
2 J. M. Tarascon and M. Armand, *Nature*, 2001, **414**, 359–367.
3 Y. K. Sun, *ACS Energy Lett.*, 2017, **2**, 2694–2695.
4 J. Hassoun, K. S. Lee, Y. K. Sun and B. Scrosati, *J. Am. Chem. Soc.*, 2011, **133**, 3139–3143.
5 H. Kim, J. Hong, K. Y. Park, H. Kim, S. W. Kim and K. Kang, *Chem. Rev.*, 2014, **114**, 11788–11827.
6 H. Nishide and K. Oyaiz, *Science*, 2008, **319**, 737.
7 P. Yadav, N. Kumari and A. K. Rai, *J. Power Sources*, 2023, **555**, 232385.
8 J. Singh, S. Lee, Zulkifli, J. Kim and A. K. Rai, *J. Alloys Compd.*, 2022, **920**, 165925.
9 W. Liu, J. Hao, C. Xu, J. Mou, L. Dong, F. Jiang, Z. Kang, J. Wu, B. Jiang and F. Kang, *Chem. Commun.*, 2017, **53**, 6872–6874.
10 G. Z. Fang, J. Zhou, A. Q. Pan and S. Q. Liang, *ACS Energy Lett.*, 2018, **3**, 2480–2501.
11 A. R. Mainar, L. C. Colmenares, J. A. Blazquez and I. Urdampilleta, *Int. J. Energy Res.*, 2018, **42**, 903–918.

12 F. Wang, O. Borodin, T. Gao, X. Fan, W. Sun, F. Han, A. Faraone, J. A. Dura, K. Xu and C. Wang, *Nat. Mater.*, 2018, **17**, 543–549.

13 Y. Bai, L. Luo, W. Song, S. Man, H. Zhang and C. Ming Li, *Adv. Sci.*, 2024, 2308668.

14 Y. Bai, Y. Qin, J. Hao, H. Zhang and C. M. Li, *Adv. Funct. Mater.*, 2024, **34**, 2310393.

15 L. Y. Zhang, L. Chen, X. F. Zhou and Z. P. Liu, *Adv. Energy Mater.*, 2015, **5**, 1400930.

16 W. Li, K. Wang, S. Cheng and K. Jiang, *Energy Storage Mater.*, 2018, **15**, 14–21.

17 Y. Liang, Y. Jing, S. Gheytani, K. Y. Lee, P. Liu, A. Facchetti and Y. Yao, *Nat. Mater.*, 2017, **16**, 841–848.

18 H. Pan, Y. Shao, P. Yan, Y. Cheng, K. S. Han, Z. Nie, C. Wang, J. Yang, X. Li, P. Bhattacharya, K. T. Mueller and J. Liu, *Nat. Energy*, 2016, **1**, 16039.

19 J. Zhou, L. Shan, Z. Wu, X. Guo, G. Fang and S. Liang, *Chem. Commun.*, 2018, **54**, 4457–4460.

20 Y. Bai, H. Zhang, H. Song, C. Zhu, L. Yan, Q. Hu and C. M. Li, *Nano Energy*, 2024, **120**, 109090.

21 Y. Bai, H. Zhang, W. Liang, C. Zhu, L. Yan and C. Li, *Small*, 2023, 2306111.

22 P. Hu, M. Yan, T. Zhu, X. Wang, X. Wei, J. Li, L. Zhou, Z. Li, L. Chen and L. Mai, *ACS Appl. Mater. Interfaces*, 2017, **9**, 42717–42722.

23 F. Liu, Z. Chen, G. Fang, Z. Wang, Y. Cai, B. Tang, J. Zhou and S. Liang, *Nano-Micro Lett.*, 2019, **11**, 25.

24 C. L. Tan, X. H. Cao, X. J. Wu, Q. Y. He, J. Yang, X. Zhang, J. Z. Chen, W. Zhao, S. K. Han, G. H. Nam, M. Sindoro and H. Zhang, *Chem. Rev.*, 2017, **117**, 6225–6331.

25 L. Shi and T. Zhao, *J. Mater. Chem.*, 2017, **5**, 3735–3758.

26 X. Zhang, X. Liu, C. Yang, N. Li, T. Ji, K. Yan, B. Zhu, J. Yin, J. Zhao and Y. Li, *Surf. Coat. Technol.*, 2019, **358**, 661–666.

27 X. Wang, Y. Huang, D. Jia, W. Pang, Z. Guo, Y. Du, X. Tang and Y. Cao, *Inorg. Chem.*, 2015, **54**, 11799–11806.

28 S. H. Lee, H. M. Cheong, M. J. Seong, P. Liu, C. E. Tracy, A. Mascarenhas, J. R. Pitts and S. K. Deb, *Solid State Ion.*, 2003, **165**, 111–116.

29 N. M. Abd-Alghafour, G. A. Naeem and S. M. Mohammad, *J. Phys.: Conf. Ser.*, 2020, **1535**, 012046.

30 H. Yin, C. Song, Y. Wang, S. Li, M. Zeng, Z. Zhang, Z. Zhu and K. Yu, *Electrochim. Acta*, 2013, **111**, 762–770.

31 Z. Chen, J. Hu, S. Liu, H. Hou, G. Zou, W. Deng and X. Ji, *Chem. Eng. J.*, 2021, **404**, 126536.

32 L. Shan, J. Zhou, W. Zhang, C. Xia, S. Guo, X. Ma, G. Fang, X. Wu and S. Liang, *Energy Technol.*, 2019, **7**, 1900022.

33 C. Liu, M. Tian, M. Wang, J. Zheng, S. Wang, M. Yan, Z. Wang, Z. Yin, J. Yang and G. Cao, *J. Mater. Chem. A*, 2020, **8**, 7713–7723.

34 Y. Li, Z. Huang, P. K. Kalambate, Y. Zhong, Z. Huang, M. Xie, Y. Shen and Y. Huang, *Nano Energy*, 2019, **60**, 752–759.

35 P. Yadav, D. Putro, J. Kim and A. K. Rai, *Batteries*, 2023, **9**, 133.

36 P. Yadav, D. Putro, N. Kumari, J. Kim and A. K. Rai, *Phys. Chem. Chem. Phys.*, 2023, **25**, 21082–21088.

37 N. Zhang, Y. Dong, M. Jia, X. Bian, Y. Wang, M. Qiu, J. Xu, Y. Liu, L. Jiao and F. Cheng, *ACS Energy Lett.*, 2018, **3**, 1366–1372.